Comparisons Between the Field Lines Using an Accelerating and a Constant Solar Wind model

Comparisons Between the Field Lines Using an Accelerating and a Constant Solar Wind model

S. Tasnim[1], Iver H. Cairns[2], M. S. Wheatland[2], B. Li[2], and Gary P. Zank[1]

[1] Center for Space Plasma and Aeronomic Research (CSPAR), University of Alabama in Huntsville, Huntsville, AL 35805, USA
[2] School of Physics, The University of Sydney, NSW-2006, Australia

E-mail: samira.tasnim@uah.edu, iver.cairns@sydney.edu.au, michael.wheatland@sydney.edu.au, garyp.zank@gmail.com

Abstract. Magnetic field line mapping between the Sun and the Earth is important to trace the nonthermal particles. We generalize a recently developed mapping approach (**B** stepping) where this approach allows us to map the magnetic field lines by stepping along the local magnetic field direction. We employ an advanced solar wind model which includes acceleration, angular momentum conservation, and intrinsic non-radial velocities and magnetic fields at the inner boundary /source surface. We map the field lines using Wind spacecraft data for two solar rotation periods: one near a solar minimum between CR2118 and CR2119 and other CR1992 near a solar maximum. Maps using the accelerating solar wind model are compared with the maps using a constant solar wind model. On a broad scale, maps using two solar wind models for the same solar rotation periods are very similar. However, in a small scale, there are significant differences, e.g. differences are evident in connectivities, paths, and winding angles. In addition, field lines using the accelerating solar wind model are more azimuthally oriented for during the solar maximum. These differences demonstrate the significance of inclusion of the accelerating radial speed profile, intrinsic azimuthal velocity and magnetic field components.

1. Introduction

The heliospheric magnetic field structure and configuration help us to study and understand the transport of the nonthermal particles and solar wind's source regions (Feldman et al. 1975, Rosenbauer *et al.* 1977, Owens & Forsyth 2013). Nonthermal particles, e.g. suprathermal Strahl electrons with energy $\approx 80\,\mathrm{eV} - 2\,\mathrm{keV}$ (Rosenbauer *et al.* 1977), solar energetic particles (SEPs) with energy 1 MeV (Kutchko et al. 1982, Richardson et al. 1991, Ruffolo *et al.* 2006), and the subrelativistic to relativistic electrons that produce type III solar radio bursts (Suzuki & Dulk 1985, Reiner et al. 1995)), are much faster than convective velocity $\mathbf{E} \times \mathbf{B}$ and the thermal particle. This results in the nonthermal particle to trace easily the magnetic field line structure (Schatten et al. 1968, Owens & Forsyth 2013, Li et al. 2016a,b).

Parker first explained that the rotation of the Sun naturally produces spiral like magnetic field structure (Parker 1958). The magnetic field lines are observed to follow Parker spiral when we averaged them over many solar rotation periods. However, in the short time-scale, they show significant deviations from the Parker spiral (Forsyth et al. 1996, Borovsky 2010, Schulte in den Bäumen et al. 2011, 2012, Tasnim & Cairns 2016, Tasnim et al. 2018). Moreover, complex

magnetic field structures are often observed by tracing the solar energetic particles, relativistic electrons, and protons (Suzuki & Dulk 1985, Owens & Forsyth 2013).

Various solar wind models are proposed to explain the deviations from Parker spiral (Fisk 1996, Gosling & Skoug 2002, Schwadron et al. 2010, Smith 1979, Schulte in den Bäumen et al. 2011, 2012, Tasnim & Cairns 2016, Tasnim et al. 2018). Besides, a number of mapping approaches are developed to predict the field lines from close to the Sun to the Earth's location (Schatten et al. 1968, Nolte & Roelof 1973*b*,*a*, Li et al. 2016a,b). Ecliptic magnetic field was first mapped on a large scale by Schatten et al. (1968), where they employed the near-Earth spacecraft data. The field lines using the solar maximum data were observed to have more structures, whereas these lines are observed to be more open near the solar minimum (Schatten et al. 1968). Later, Nolte & Roelof (1973*b*,*a*) showed that the longitudes of the source surface are related to the longitudes of the observed magnetic field data. However, these approaches are failed to distinguish between the open and closed field lines (Gosling & Roelof 1974).

A recently developed mapping approach Li et al. (2016a) employ an equatorial two dimensional solar wind model of Schulte in den Bäumen et al. (2012) and 1 AU near Earth data to predict the field lines from the source surface to 1 AU. Note that Schulte in den Bäumen et al. (2012)'s model includes an intrinsic azimuthal magnetic field component. The predicted field lines agreed 90% with the observed pitch angle distribution data (Li et al. 2016a). In further research, they extended the work to predict the correlation between the path of subrelativistic electrons of the Type III radio burst and the path of the magnetic field lines. They also compare them with the observed field line inversion in the equatorial plane. However, all the above mapping approaches employed solar wind models where the solar wind's radial speed is constant along the radial distance.

In this paper, we employ an advanced generalized solar wind model which includes an accelerating radial wind profile, intrinsic azimuthal magnetic field, and angular momentum conservation. In addition, the model includes a deviation from corotation, which results in an intrinsic azimuthal velocity (Tasnim et al. 2018). We improve **B**-step algorithm developed by Li et al. (2016a) and Li et al. (2016b) and map the field lines which are not only biased along the 1 AU. This model also uses 1 AU near Earth data from the Wind spacecraft. We predict the field lines for two solar rotations, one near the solar maximum and another the solar minimum. Note that Tasnim et al. (2018)'s model does not consider dynamical variations between the source surface and 1 AU. However, the non-Parker like magnetic field structure and the large values of the observed azimuthal velocity at 1 AU can be due to dynamic effects as stream-stream interactions (SIRs) at corotating interaction regions (CIRs) (Hu & Habbal 1992, Hu 1993, Odstřcil 1994, Richardson et al. 1996).

This paper is structured as follows. Section 2.1 briefly expresses and describes the magnetic field components using the accelerating solar wind model of Tasnim et al. (2018) whereas Section 2.2 describes the magnetic field components using the constant solar wind model of Schulte in den Bäumen et al. (2012). The predicted magnetic field components are used to extract the magnetic field vectors for both of the models. Section 3 provides a short description of the modified **B**-stepping ((Li et al. 2016a), (Li et al. 2016b)) approach. Section 4 qualitatively and quantitatively describes magnetic field lines using two solar wind models. Section 5 gives a brief discussion of the results and concludes the paper.

2. Solar Wind Models and Predictions

2.1. Magnetic Field Components using an Advanced Data Driven Accelerating Solar Wind Model

We use Tasnim et al. (2018)'s data driven equatorial accelerating solar wind model to extract the radial and azimuthal magnetic field components. The above model includes Parker's accelerating radial speed profile using an implicit method along with intrinsic non-radial

velocities and magnetic fields at the inner boundary/source surface. The model uses several magnetodyhrodynamic (MHD) equations: (a) frozen-in field equation, (b) angular momentum conservation equation $\partial L_\star/\partial t + \rho \mathbf{r} \times (\mathbf{v} \cdot \nabla)\mathbf{v} = (1/\mu_0)\mathbf{r} \times (\mathbf{B} \cdot \nabla)\mathbf{B} = 0$ by assuming a radially symmetric thermal and magnetic pressure, (c) conservation of mass $\rho(r)v_r(r)r^2 =$ constant, (d) Gauss's Law $\nabla \cdot \mathbf{B} = 0$, and (e) Faraday's Law $\nabla \times \mathbf{E}' = 0$ assuming a time stationary electric field in the rotating frame. Here ρ is the mass density, t is the time, $\mathbf{v}$ is the velocity, $\mathbf{E}$ is the electric field, and $\mathbf{B}$ is the magnetic field.

The accelerating solar wind model of Tasnim et al. (2018) considers that the solar wind pattern is constant over a solar rotation period. This assumption allows the fixed pattern to rotate with the Earth and to vary the wind radially and longitudinally. We assume the magnetic field and velocity have radial and azimuthal components in the equatorial plane, i.e. $\mathbf{B} = (B_r, B_\phi)$ and $\mathbf{v} = (v_r, v_\phi)$. Here v_r and v_ϕ are the radial and azimuthal components of the velocity whereas B_r and B_ϕ are the radial and azimuthal components of the magnetic field. We assume the non-radial component of the magnetic field is constant along the longitudinal direction locally, i.e. $\partial B_\phi/\partial\phi = 0$. Detailed description and derivation is provided in Tasnim et al. (2018). We use primed variables to present the plasma quantities and magnetic field components in the corotating frame. Above assumptions yield the following expression for the radial magnetic field:

$$r'^2 B'_r(r', \phi') = r^2 B_r(r, \phi, t) = r'^2_{\rm s} B'_r(r'_{\rm s}, \phi'_{\rm s}). \tag{1}$$

Similarly, we can derive the expression for the azimuthal magnetic field at any location (r, ϕ) which provides

$$B_\phi(r', \phi') = B_\phi(r, \phi, t) = \frac{r_{\rm s} v_r(r_{\rm s}, \phi_{\rm s}, t) B_\phi(r_{\rm s}, \phi_{\rm s}, t)}{r v_r(r, \phi, t)} - \frac{r_{\rm s} \delta v_\phi(r_{\rm s}, \phi_{\rm s}, t) B_r(r_{\rm s}, \phi_{\rm s}, t)}{r v_r(r, \phi, t)} + \frac{v_\phi(r, \phi, t) B_r(r, \phi, t)}{v_r(r, \phi, t)} - \frac{\Omega r_{\rm s}^2 B_r(r_{\rm s}, \phi_{\rm s}, t)}{r v_r(r, \phi, t)}, \tag{2}$$

where $r_{\rm s}$ defines the radial distance of the source surface or the inner boundary of the solar wind. Note that we define the source surface/inner-boundary as a locus where the solar wind originates from. Here $\Omega = 2\pi/T$ presents the Sun's rotation frequency, $T = 27$ days $= 648$ hours is synodic rotation period of the Sun. In addition, $v_r(r_{\rm s}, \phi_{\rm s}, t)$ is the radial velocity at the source surface, $\delta v_\phi(r_{\rm s}, \phi_{\rm s}, t)$ is the deviation from corotation, $v_\phi(r, \phi, t)$ and $v_r(r, \phi, t)$ are the azimuthal and radial velocities at any location (r, ϕ) at any time t of the solar rotation period, $B_r(r, \phi, t)$ is the radial magnetic field at (r, ϕ) and time t.

2.2. Magnetic Field Components for a Constant Radial Speed Solar Wind Model

We use Schulte in den Bäumen et al. (2012)'s model which was previously employed by Li et al. (2016a) and Li et al. (2016b) to map the magnetic field lines. This model assumes a constant radial speed and includes an intrinsic azimuthal magnetic field component at the inner boundary / source surface. We re-write the original equations in a corotating frame to make the magnetic field components consistent with those from Section 2.1. Note that Schulte in den Bäumen et al. (2012)'s model does not include the intrinsic azimuthal velocity or deviation from the corotation.

The radial magnetic field component for the Schulte in den Bäumen et al. (2012) model is same as for the Tasnim et al. (2018)'s model. In addition, the expression for the azimuthal component of the magnetic field is:

$$B_\phi(r', \phi') = B_\phi(r, \phi, t) = \frac{B_\phi(r_{\rm s}, \phi_{\rm s}, t) r_{\rm s}}{r} - \frac{B_r(r, \phi, t)\Omega(r - r_{\rm s})}{v_r(\phi, t)}. \tag{3}$$

2.3. Extraction of the Plasma Quantities and Magnetic Field Components
We use 1 AU data from the Wind Spacecraft and fit them with the model predictions to extract $B'_\phi(r'_s, \phi'_s)$, $B'_r(r'_s, \phi'_s)$, and $\delta v_\phi(r'_s, \phi'_s)$. Then, we predict $B'_r(r', \phi') = B_r(r, \phi, t)$ and $B'_\phi(r', \phi') = B_\phi(r, \phi, t)$ using the above expressions and 1 AU data at any (r, ϕ) location of the equatorial plane.

3. B-step Mapping Approach
We improve Li et al. (2016a,b)'s mapping algorithm to display and provide a "global" and unbiased magnetic field map where the field lines are not only biased around 1 AU. The updated algorithm is applicable to map the field lines at any radial and longitudinal location instead of field lines around 1 AU. We also name it as the B-step algorithm since we map the lines by stepping along the local magnetic field, i.e. the lines step along $\mathbf{B}$ and $-\mathbf{B}$ from a starting point $\mathbf{r}_0 = (x_0, y_0)$ in the equatorial plane between the Sun and the Earth.

The field line locations are calculated by averaging over four neighbouring local points to move toward a new point $r = (x, y)$ which can be expressed as

$$x = x_0 + \Delta x = x_0 + \sum_{i=1}^{4} \frac{B_{xi}}{B_i} dl \ , \tag{4}$$

$$y = y_0 + \Delta y = y_0 + \sum_{i=1}^{4} \frac{B_{yi}}{B_i} dl \ , \tag{5}$$

where x and y components of the magnetic field vectors are defined by B_{xi} and B_{yi} with $i = 1, 2, 3,$ and, 4 for the four nearest neighbouring points. These field lines start from an initial starting point $\mathbf{r}_0$ and step toward a new point $\mathbf{r}_i$. The process continues still the field lines reach the chosen end point. The mapping procedure continues in the opposite direction by the conversions $(\Delta x, \Delta y) \rightarrow (-\Delta x, -\Delta y)$ along with $dl \rightarrow -dl$ in Equations 4 - 5. These equations completely satisfy the Gauss's Law, but do not preserve the direction $\mathbf{B}$ at 1 AU which is due to fact that above equations use a local average instead of using an interpolated data.

4. Field Line Maps for the Accelerating and the Constant Radial Speed Wind
This section describes the detailed structures and orientations of the magnetic field lines for an accelerating and a constant solar wind and discusses the qualitative correlation between observed data at 1 AU using the Wind Spacecraft data for the solar rotation period 6 December 2011 and 1 January 2012 (between CR 2118 – CR 2119) near a solar minimum and another solar rotation period near a solar maximum from 1 July 2002 to 27 July 2002 (CR1992). We define the antisunward direction with angles $90° \leq \Phi_B \leq 270°$ and the remaining angles as (within 360° rotation) sunward ($0° \leq \phi_B < 90°$ or $270° < \phi_B \leq 360°$) direction, where ϕ_B is the in-ecliptic angle and $\phi_B = \tan^{-1}(B_\phi/B_r)$. Parker spiral model restricts ϕ_P between $90° < \Phi_B < 180°$ or $270° < \phi_P < 360°$, where ϕ_P is the Parker spiral angle. Mapping algorithm also allows the field lines to orient approximately radial and even sometimes to orient anticlockwise direction at a large heliocentric distance (an explanation is given in the following subsection). Identifications of magnetic field orientations strongly depend on the definition of the field orientations (Owens & Forsyth 2013, Li et al. 2016a,b).

4.1. Predicted Magnetic Maps Between CR2118 – CR2119: 6 December 2011 to 1 January 2012
Magnetic field line starts at 000 UT for each map in Figures 1 and 2, where the mapping lines are spaced at 8 hours interval in the Earth's orbit over the full solar rotation period. More

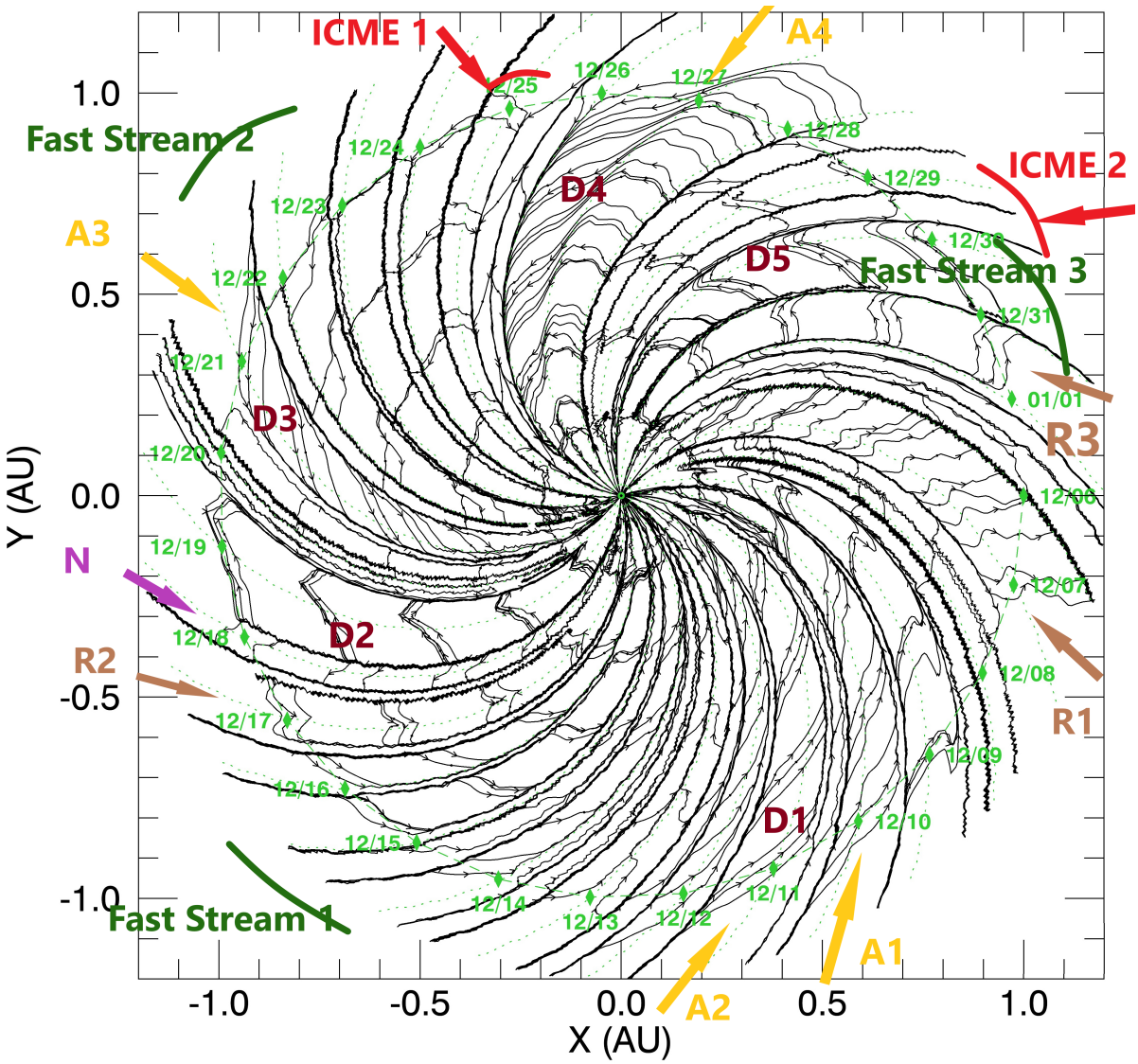

Figure 1. A map of magnetic field lines predicted using the accelerating solar wind model of Tasnim et al. (2018) in the equatorial plane for the solar rotation period between CR2118 and CR2119 (6 December 2011 and 1 January 2012). The map keeps the Sun at the center while the Earth moves around the Sun in the clockwise direction with increasing time. Here the green diamond markers show Earth's longitudinal locations every day at the universal time 0000. Inward arrows represent the inward field line, whereas outward arrows represent the opposite. Symbols Ai identify azimuthal field lines for $i = 1, 2, 3...$, and similarly Di identify the periods with low B, radial field lines as Ri, and field lines in the anticlockwise direction as N.

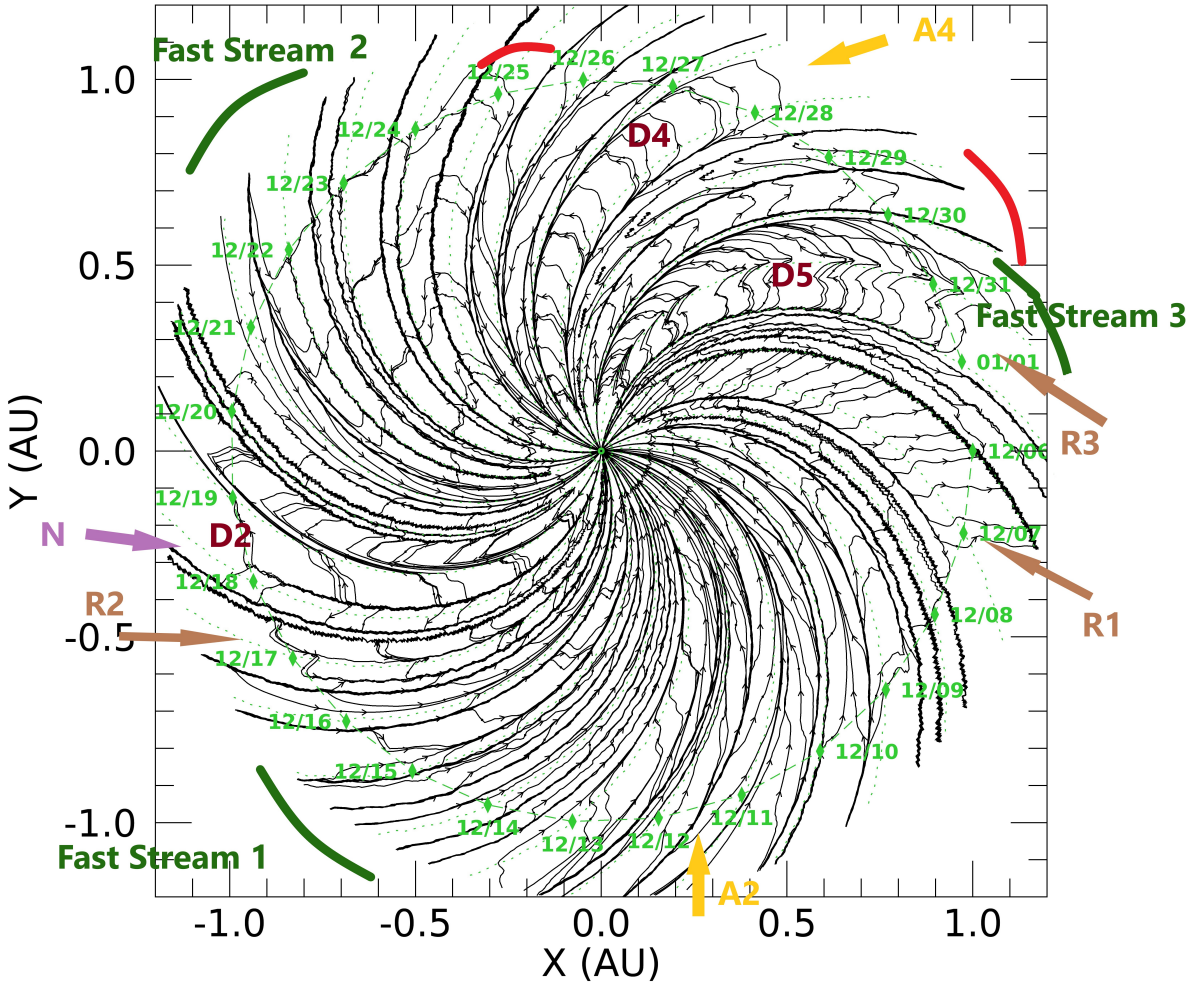

Figure 2. Magnetic field lines using the constant solar wind model of (Schulte in den Bäumen et al. 2012) for the solar rotation period between CR2118 and CR2119. Symbols have the same meaning as Figure 1.

precisely, we map the field lines at 0000 UT, 0800 UT, 1600 UT of each day. The choice of other starting points or time intervals will provide us with field lines of the remaining hours. We use definitions from Li et al. (2016a), Li et al. (2016b), and Li et al. (2016c) to describe the field lines of the accelerating $v_r(r, \phi)$ and constant v_r model (Schulte in den Bäumen et al. 2011, 2012, Li et al. 2016a,b). Several features of a solar rotation between CR2118 – CR2119 are noted below:

(i) The solar rotation contains two ICME events: ICME 1 on 25 December (0200 UT to 1700 UT) and ICME 2 between 29 to 30 December (2200 UT to 0900 UT) (Richardson & Cane 2015), and three fast stream regions: Fast Stream 1, 2, and 3 in Figures 1 and 2. These events modify the magnetic structure of the solar wind.

(ii) Figures 1 and 2 show open field lines within 24 to 25 December during the ICME event (marked as ICME 1). Note that curved red lines indicate the ICME regions. Open field lines also present in 18, 20, 21, 28, and 31 December. These lines are all sector boundaries which falsely linked as this mapping algorithm does not identify the SBs. Artificially connected lines also exist between the start and end of the solar rotation period in Figures 1 and 2.

Therefore, we assume the field lines are open when it crosses SBs and within the start and end of the solar rotation period for further analysis.

(iii) Field lines also experience the local field inversion. Figure 1 and 2 show line inversions between 21 to 22 December and between 29 to 30 December of 2011. We already mentioned that a CME event is present between 29 to 30 December (marked as ICME 2). In contrast, the inversion near 21 December is due to the presence of SIR event, which is due to the interaction between fast (labeled as Fast Stream 2) and slow streams.

(iv) Observed data and data-driven field lines magnetic show that occasionally, field lines are aligned approximately radial at large heliocentric distances (labeled as R1, R2, R3). We also see some field lines are oriented in anticlockwise direction instead of orienting in a clockwise direction like Parker spirals (labeled as N).

We now focus on similarities and dissimilarities between field lines predicted by Tasnim et al. (2018) and Li et al. (2016a,b,c). On a broad scale, Figures 1 and 2 show that magnetic maps using two solar wind models between CR2118 and CR2119 have strong similarities and some differences. Qualitative comparisons between Figure 1 and Figure 2 for the solar rotation are listed below:

(i) The field line densities are not always the same. Some days have a higher field line population than the other days. Both Figures 1 and 2 show low populated areas between 19 – 20, 26 – 28, and 30 – 31 December (labeled as D2, D4, and D5). An interpretation is that both of the solar wind models (employed to map the field lines) include intrinsic azimuthal field components $[B_\phi(r_\mathrm{s}, \phi_\mathrm{s})]$. Azimuthally oriented fields at the small heliocentric distances in both Figures 1 and 2 demonstrate the inclusion of $B_\phi(r_\mathrm{s}, \phi_\mathrm{s})$.

(ii) In addition, the map on Figure 1 shows more low populated regions than Figure 2, e.g., within 11 to 12, and 20 to 22 December (labeled as D1, and D3). The field lines are mostly azimuthal at 1 AU during this period. Additional low populated regions in the accelerating solar wind model indicates implication of the combined effect of intrinsic azimuthal velocities $\delta v_\phi(r_\mathrm{s}, \phi_\mathrm{s}) \neq 0$ and the accelerating radial wind speed $v_r(r, \phi)$. On the other hand, the constant speed model allowed a strong corotation with the Sun $\delta v_\phi = 0$ and restricted the radial speed to be constant with radial distance $v_r = v_r(\phi)$ along the velocity streamlines.

(iii) Field lines are azimuthal between 10 and 11 December and between 26 and 28 December (labeled as A1 and A4) for both of these models. However, the field lines are more azimuthal for the accelerating model. Additional azimuthally oriented field lines (marked by A2 and A3 on Figure 1) demonstrate the effect of intrinsic azimuthal velocity in Tasnim et al. (2018)'s model.

(iv) The magnetic field lines using accelerating $v_r(r, \phi)$ are sometimes disconnected close to Sun, which is due to the absence of the field vector at the Alfvénic critical radius (r_A). Tasnim et al. (2018)'s model excludes magnetic field vectors at $r_\mathrm{A}(\phi_\mathrm{A})$ to remove the singularities at $r = r_\mathrm{A}(\phi_\mathrm{A})$ when $M_A(r, \phi) = 1$. Put in other words, the accelerating solar wind excludes some points due to the presence of singularities at the Alfvénic critical point where the radial Mach number becomes 1 where the denominator in the analytic expression of the magnetic field contains a factor $(M^2_\mathrm{Ar}(r, \phi) - 1)$ [detailed description is available in Tasnim et al. (2018)]. Therefore, field line mapping stops at $r = r_\mathrm{A}(\phi_\mathrm{A})$ for predicted $\mathbf{B}$ using Tasnim et al. (2018).

(v) Variation of $r_\mathrm{A}(\phi_\mathrm{A})$ with heliolongitudes ϕ results the predicted field lines discontinuities at different radial locations [e.g. disconnected field lines $r \leq 0.2$ AU]. Note that singularities in accelerating solar wind models affect both of the algorithms. Contrarily, Schulte in den Bäumen et al. (2011, 2012)'s constant solar wind model is much simpler and only considers

frozen-in field conditions. Therefore, the model does not deal with singularity. As a result, Figure 2 shows connectivity with the source surface.

(vi) Field line connections in maps of Figures 1 and 2 between 6 December of 2011 and 1 January of 2012 indicate that **B**-step approach artificially connects field lines at the start and end of the solar rotation period.

Figure 3 shows field lines between 8 to 10 December (top two panels) and 24 and 29 December (bottom two panels) 2011. Field lines on the left-hand side are using the accelerating solar wind model, and the lines on the right-hand side are using the constant solar wind model. These lines explicitly show a notable path and connectivity differences. Dissimilarities in field-line connections and traveled paths indicate that the inclusion of acceleration and intrinsic non-radial velocity significantly changes the field line structures, even though their orientations at 1 AU remain very similar. As a result, field line orientations at 1 AU are categorized in the same PAD classes for both of the solar wind models.

4.2. Maps Between 1 July and 27 July 2002 (CR1992)

Figures 4 and 5 show the maps for a solar rotation period CR1992 near a solar maximum. The Wind Spacecraft data for the period shows the existence of of two ICMEs (ICME 1 between 18 July to 19 July and ICME 2 between 20 July to 22 July) (Richardson & Cane 2015) and three fast streams.

Field lines for the accelerating and constant solar wind models have strong similarities as like the corresponding maps for the solar minimum. However, Figure 4 shows more azimutally oriented field lines for accelerating solar wind models during the period near solar maximum than for the solar minimum. One interpretation is probably partly due to the existence of solar activities between CR1992 over a longer period than the solar rotation period between CR2118 and CR2119. For instance, field lines between 9 – 10, 16 – 19, and 20 – 23 July of 2002. Yellow arrows labeled as A1, A2, A3, A4, and A5 also indicate that the influence of deviation of corotation or intrinsic azimuthal velocities is more dominating during the solar maximum. Note that all the symbols have the same meaning as like Figure 1.

Figure 5 shows few filed lines between 6 to 11 July (top panels) and 13 to 17 July (bottom panels) of 2002 for the accelerating (left panels) and the constant (right panels) solar wind models near 1 AU. These fields lines clearly show that intrinsic azimuthal velocity strongly affects the path of the field lines during the solar maximum than during the solar minimum.

5. Discussion and Conclusions

This paper improves the **B**-stepping mapping algorithm of Li et al. (2016a) to provide an unbiased and complete magnetic map for any starting point at any radial and longitudinal location from the source surface to 1 AU and even beyond.

The primary achievement of this paper is the application of an advanced solar wind model, which includes acceleration of the solar wind, intrinsic azimuthal velocity by allowing a deviation from the strong corotation along with a non-zero azimuthal intrinsic magnetic field. More precisely, this work generalizes the mapping approach of Li et al. (2016a,b) with a more advanced solar model. Mapped field lines are very similar for both of these models; notably, they have the same orientation at 1 AU.

Another importance of this work apart from generalising the analyses of Li et al. (2016a,b) to a new solar wind model, is that the very similar results in Figures 1 and 2 suggest that the comprehensive testing of Li et al. (2016a,b) against observational data will apply with minimal changes to use of the accelerating wind model. Thus, further work or mapping lines in the solar wind can confidently use Tasnim et al. (2018) new accelerating wind model instead of the simpler Schulte in den Bäumen et al. (2011, 2012) model used by Li et al. (2016a,b).

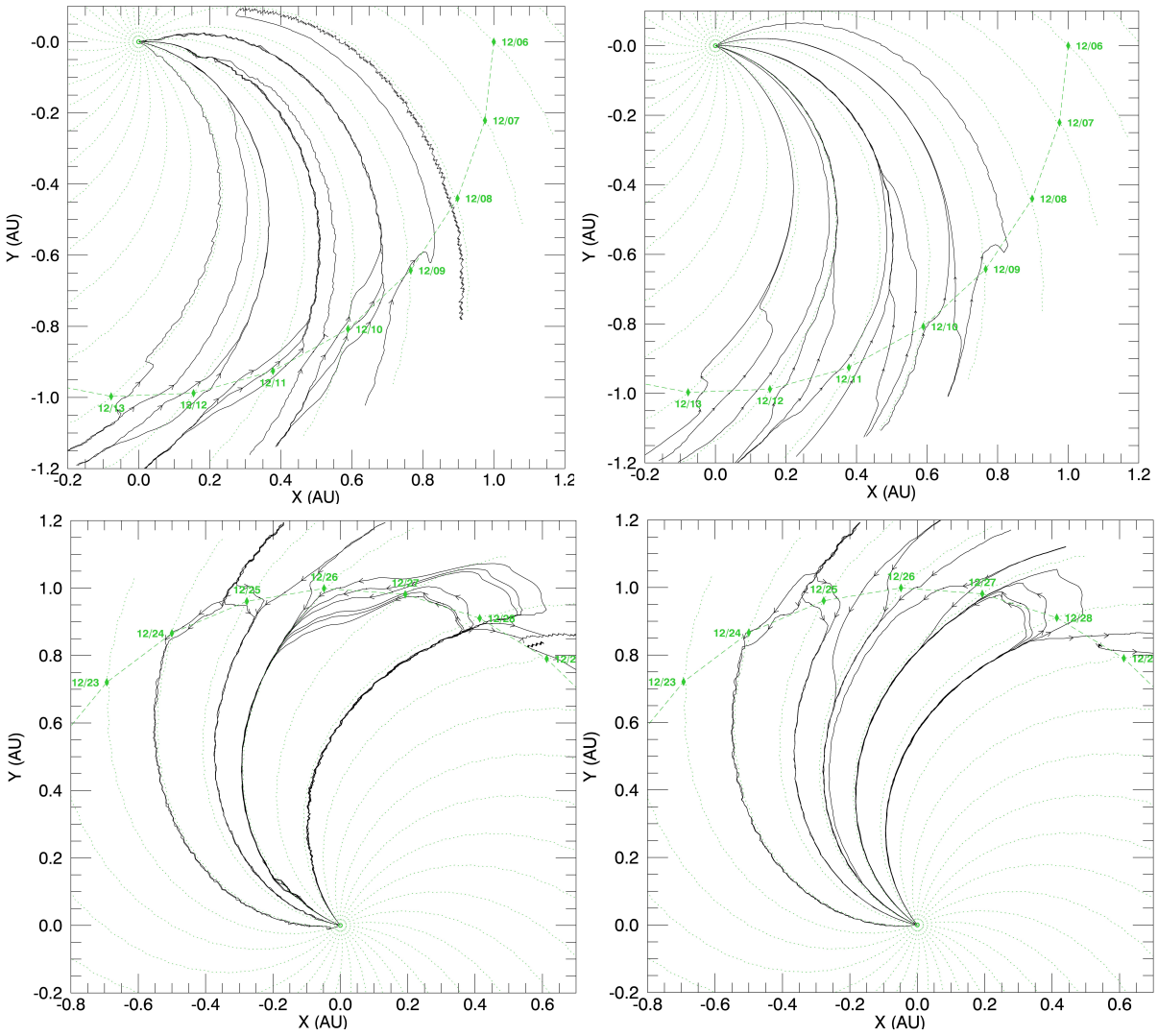

Figure 3. The predicted magnetic field lines between 8 to 13 December 2011 (top panels) for the accelerating (left) and the constant (right) wind models. Similarly, the lines between 24 to 26 December 2011 are shown in bottom panels for the accelerating (left) and the constant (right) solar wind models.

In summary, maps from two solar wind models are similar in a broad-scale. However, close observations of these maps show that the magnetic field lines for the accelerating radial speed model (Figure 1) and the constant radial speed wind model (Figure 2) have a notable path and connectivity differences. See, for instance, the almost horizontal field lies near 1 AU at the top of each map. These dissimilarities suggest that the inclusion of acceleration of the radial speed and intrinsic non-radial velocity have significant effects on magnetic field lines. This result agrees with the analytic expression of the magnetic field components where field components are correlated to the velocity components.

Maps in Figure 1 and 2 also demonstrate that the field lines do not always follow velocity streams. The success rate for predicting magnetic field lines for Tasnim et al. (2018)'s model is little different than the constant radial speed model from Li et al. (2016a) and Li et al. (2016b).

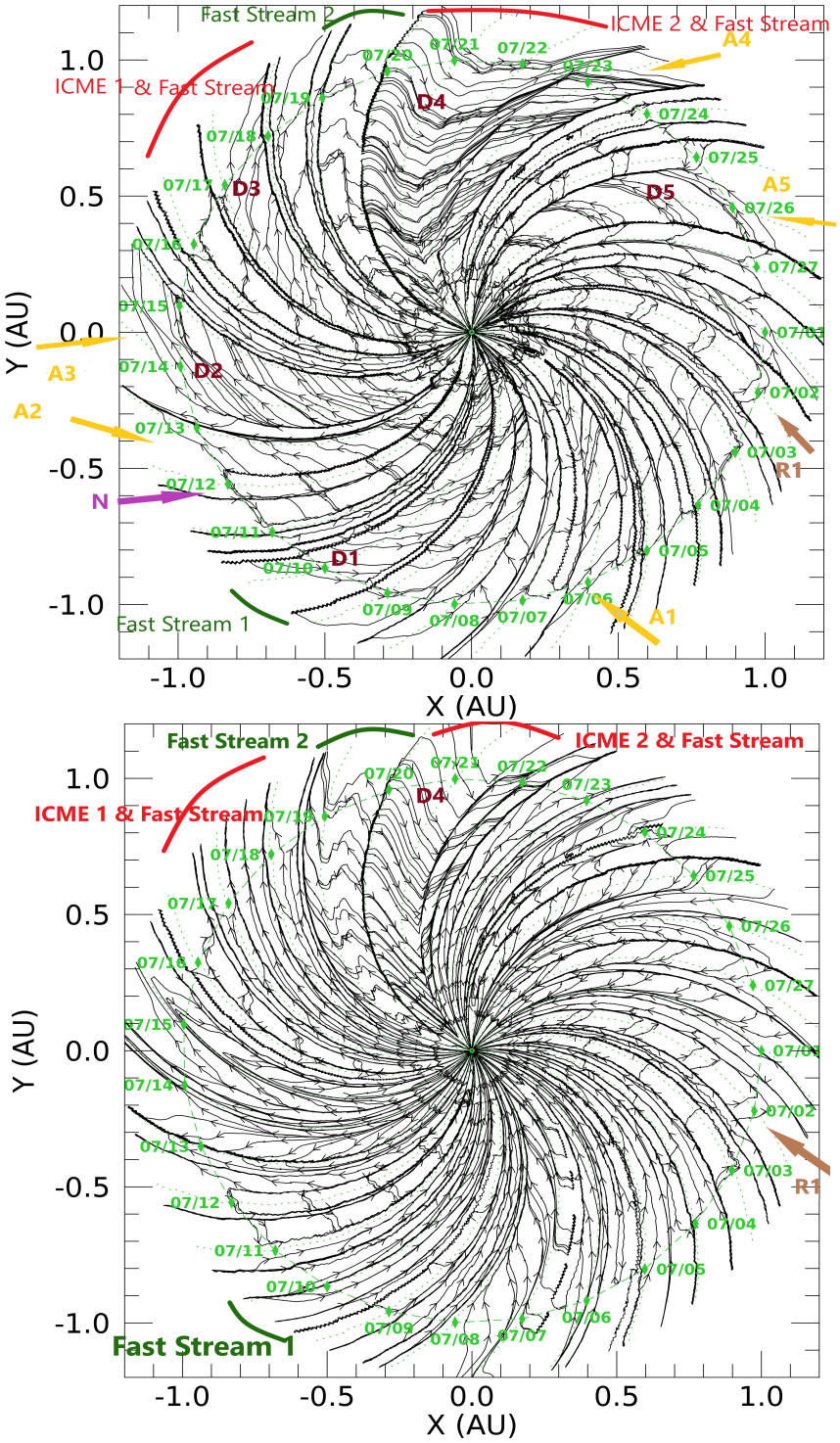

Figure 4. Predicted magnetic field line maps for the solar rotation period 1 July to 27 July 2002 (CR 1992) using the accelerating solar wind model of Tasnim et al. (2018) (top) and the constant solar wind model of Schulte in den Bäumen et al. (2012) (bottom).

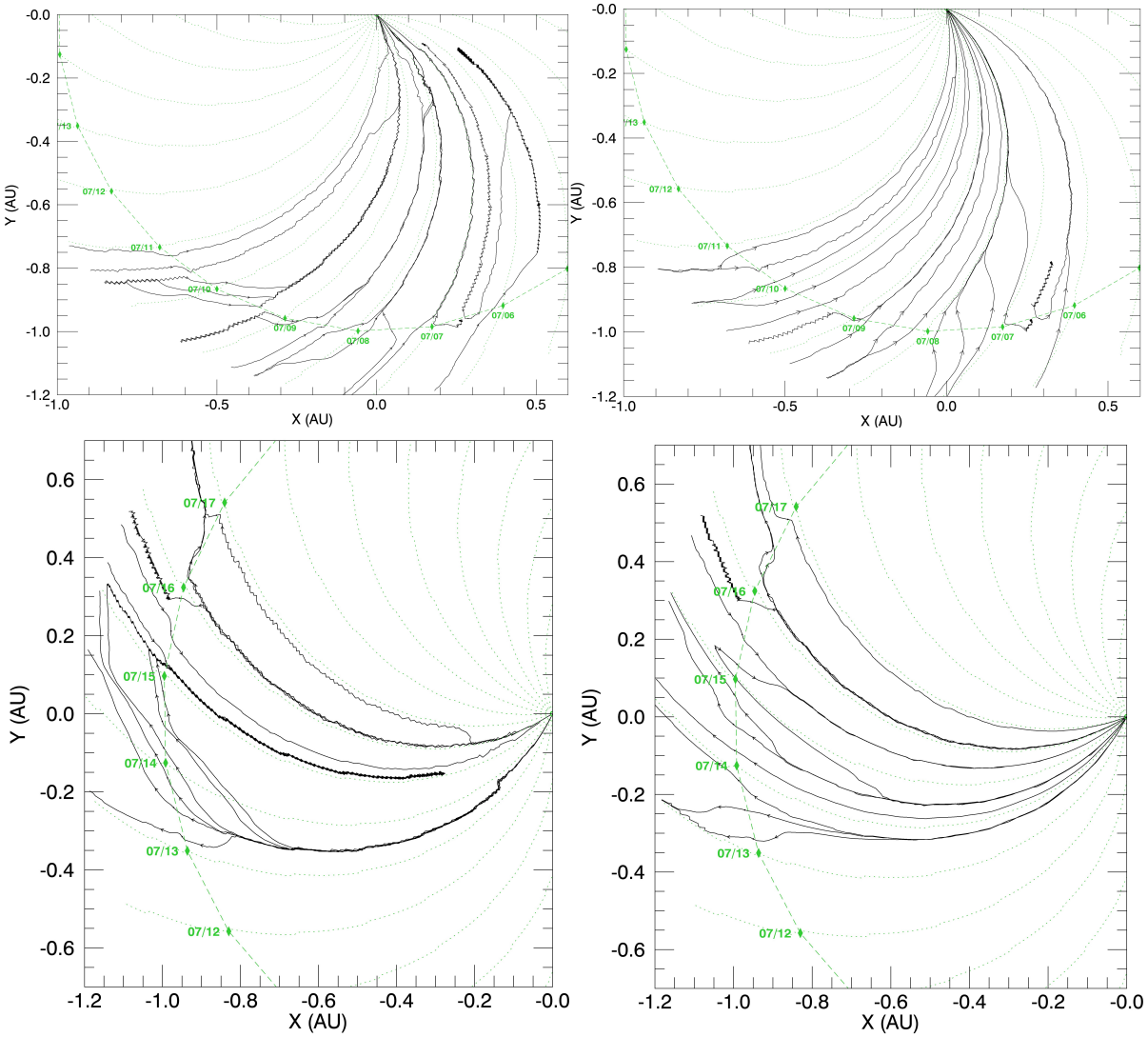

Figure 5. The predicted field lines between 6 to 11 July (top panels) and 13 to 17 July of 2002 (bottom panels) where the left two panels show the lines for the accelerating solar wind model and the right two panels shows the lines for a constant solar wind model.

Acknowledgments

G.P.Z. acknowledge the partial support of an NSF DOE grant PHY - 1707247 and a NASA grant SV4 - 84017. This material is based also in part upon work supported by the NSF EPSCoR RII-Track-1 Cooperative Agreement OIA-1655280. G.P.Z. acknowledges the generosity of the International Space Science Institute (ISSI) in supporting him through the 2017 Johannes Geiss Fellowship. This work is also partly supported by the International Space Science Institute (ISSI) in the framework of International Team 504 entitled Current Sheets, Turbulence, Structures and Particle Acceleration in the Heliosphere. We thank Jakobus le Roux for the useful discussion. The simulations are performed at Los Alamos National Laboratory.

References

Borovsky, J. E. (2010), 'On the variations of the solar wind magnetic field about the Parker spiral direction', *J. Geophys. Res.* **115**, A09101. doi: 10.1029/2009JA015040.

Feldman, W. C., Asbridge, J. R., Bame, S. J., Montgomery, M. & Gary, S. P. (1975), 'Solar wind electrons', *J. Geohys. Res.* **80**, 4181–4196. doi: 10.1029/JA080i031p04181.

Fisk, L. A. (1996), 'Motion of the footpoint of the heliospheric magnetic field lines at the sun: Implications for recurent energetic particle events at high heliographic latitude', *J. Geophys. Res.* **101**, 547. doi: 10.1029/96JA01005.

Forsyth, R. J., Balogh, A., Horbury, T. S., Erdos, G., Smith, E. J. & Burton, M. E. (1996), 'The heliospheric magnetic field at solar minimum: Ulysses observations from pole to pole', *Astron. Astrophys.* **316**, 287.

Gosling, J. T. & Roelof, E. C. (1974), 'A comment on the detection of closedmagnetic structures in the solar wind', *Sol. Phys.* **39**, 405408. doi: 10.1007/BF00162433.

Gosling, J. T. & Skoug, R. M. (2002), 'On the origin of radial magnetic fields in the heliosphere', *J. Geophys. Res.* **107(A10)**, 1327. doi: 10.1029/2002JA009434.

Hu, Y. Q. (1993), 'Evolution of corotating stream structures in the heliospheric equatorial plane', *J. Geophys. Res.* **98**, 13,201–13,214.

Hu, Y. Q. & Habbal, S. R. (1992), 'Double shock pairs in the solar wind', *J. Geophys. Res.* **98**, 3551.

Kutchko, F. J., Briggs, P. R. & Armstrong, T. P. (1982), 'The bidirectional particle event of October 12, 1977, possibly associated with a magnetic loop', *J. Geophys. Res.* **82**, 14191431. doi: 10.1029/JA087iA03p01419.

Li, B., Cairns, I. H., Gosling, J. T., Malaspina, D., Neudegg, D., Steward, G. & Lobzin, V. (2016b), 'Comparisons of mapped magnetic field lines with the source path of the 7 April 1995 type III solar radio burst', *J. Geophys. Res.* **121**, 61416156. doi: 10.1002/2016JA022756.

Li, B., Cairns, I. H., Gosling, J. T., Steward, G., Francis, M., Neudegg, D., in den Bumen, H. S., Player, P. R. & Milne, A. (2016a), 'Mapping magnetic field lines between the Sun and Earth', *J. Geophys. Res.* **121**, 925–948. doi: 10.1002/2015JA021853.

Li, B., Cairns, I. H., Owens, M. J., Neudegg, D., Lobzin, V. V. & Steward, G. (2016c), 'Magnetic field inversions at 1 AU: Comparisons between mapping predictions and observations', *J. Geophys. Res.* **121**, 1072810743. doi: 10.1002/2016JA023023.

Nolte, J. T. & Roelof, E. C. (1973*a*), 'Large-scale structure of the interplanetary medium i: High coronal source longitude of the quite-time solar wind', *Sol. Phys.* **33**, 241–257. doi: 10.1007/BF00152395.

Nolte, J. T. & Roelof, E. C. (1973*b*), 'Large-scale structure of the interplanetary medium II: Evolving magnetic configurations deduced from multi-spacecraft observations', *Sol. Phys.* **33**, 483–504. doi: 10.1007/BF00152435.

Odstřcil, D. (1994), 'Interactions of solar wind streams and related small structures', *J. Geophys. Res.* **99**, 17,653–17,671.

Owens, M. J. & Forsyth, R. J. (2013), 'The heliospheric magnetic field', *Living Rev. Solar Phys.* **10**, 5. doi: 10.12942/lrsp-2013-5.

Parker, E. N. (1958), 'Dynamics of the interplanetary gas and magnetic fields', *Z. Astrophys* **29**, 274. doi: 10.1086/146579.

Reiner, M. J., Fainberg, J. & Stone, R. G. (1995), 'Large-scale interplanetarymagnetic field configuration revealed by solar radio bursts', *Science* **270**, 461464. doi: 10.1126/science.270.5235.461.

Richardson, I. G. & Cane, H. V. (2015), 'Near-Earth interplanetary coronal mass ejections since january 1996', http://www.srl.caltech.edu/ACE/ASC/DATA/level3/icmetable2.htm. [Updated September 22, 2015].

Richardson, I. G., Cane, H. V. & von Rosenvinge, T. T. (1991), 'Prompt arrival of solar energetic particles from far eastern events The role of large-scale interplanetarymagnetic field structure', *J. Geophys. Res.* **96**, 78537786. doi: 10.1029/2011GL049578.

Richardson, J. D., Belcher, J. W., Lazarus, A. J., Paularena, K. I., Steinberg, J. T. & Gazis, P. R. (1996), 'Non-radial flows in the solar wind', *AIP Conf. Proc.* **382**, 479.

Rosenbauer *et al.*, H. (1977), 'A survey on initial results of the helios plasma experiment', *J. Geohys.* **42**, 561580.

Ruffolo *et al.*, D. (2006), 'Relativistic solar protons on 1989 October 22: Injection and transport along both legs of a closed interplanetary magnetic loop', *Astrophys. J.* **639**, 1186. doi: 10.1086/499419.

Schatten, K. H., Ness, N. F. & Wilcox, J. M. (1968), 'Influence of a solar active region on the interplanetary magnetic field', *Sol. Phys.* **5**, 240–256. doi: 10.1007/BF00147968.

Schulte in den Bäumen, H., Cairns, I. H. & Robinson, P. A. (2011), 'Modeling 1 AU solar wind observations to estimate azimuthal magnetic fields at the solar source surface', *Geophys. Res. Lett.* **38**, L24101. doi: 10.1029/2011GL049578.

Schulte in den Bäumen, H., Cairns, I. H. & Robinson, P. A. (2012), 'Nonzero azimuthal magnetic fields at the solar source surface: Extraction, model, and implications', *J. Geophys. Res.* **117**, 104. doi: 10.1029/2012JA017705.

Schwadron, N. A., Connick, D. E. & Smith, C. W. (2010), 'Magnetic flux balance in the heliosphere', *Astrophys. J. Lett.* **722**, L132. doi: 10.1088/2041-8205/722/2/L132.

Smith, E. J. (1979), 'Interplanetary magnetic fields', *Rev. Geophys* **17**, 610. doi: 10.1029/RG017i004p00610.

Suzuki, S. & Dulk, G. A. (1985), *Bursts of type III and type V, in Solar Radiophysics*, Cambridge (U. K.).

Tasnim, S. & Cairns, I. H. (2016), 'An equatorial solar wind model with angular momentum conservation and non-radial magnetic fields and flow velocities at an inner boundary', *J. Geophys. Res.* **121**, 4966–4984. doi: 10.1002/2016JA022725.

Tasnim, S., Cairns, I. H. & Wheatland, M. S. (2018), 'A generalized equatorial model for the accelerating solar wind', *J. Geophys. Res.* **123**, 1061–1085. doi: 10.1002/2017JA024532.